Measuring Velocities in the Early Stage of an Eruption: Using "Overlappogram" Data from *Hinode* EIS

Louise K. Harra[1], Hirohisa Hara[2], George A. Doschek[3], Sarah Matthews[1], Harry Warren[3],
J. Leonard Culhane[1], and Magnus M. Woods[1]

[1] UCL-Mullard Space Science Laboratory Holmbury St Mary, Dorking, Surrey, RH5 6NT, UK; l.harra@ucl.ac.uk
[2] National Astronomical Observatory of Japan, Osawa, Mitaka, Tokyo 181-8588, Japan
[3] Space Science Division, Naval Research Laboratory, 4555 Overlook Avenue, SW, Washington, DC 20375, USA

Abstract

In order to understand the onset phase of a solar eruption, plasma parameter measurements in the early phases are key to constraining models. There are two current instrument types that allow us to make such measurements: narrow-band imagers and spectrometers. In the former case, even narrow-band filters contain multiple emission lines, creating some temperature confusion. With imagers, however, rapid cadences are achievable and the field of view can be large. Velocities of the erupting structures can be measured by feature tracking. In the spectrometer case, slit spectrometers can provide spectrally pure images by "rastering" the slit to build up an image. This method provides limited temporal resolution, but the plasma parameters can be accurately measured, including velocities along the line of sight. Both methods have benefits and are often used in tandem. In this paper we demonstrate for the first time that data from the wide slot on the *Hinode* EUV Imaging Spectrometer, along with imaging data from AIA, can be used to deconvolve velocity information at the start of an eruption, providing line-of-sight velocities across an extended field of view. Using He II 256 Å slot data at flare onset, we observe broadening or shift(s) of the emission line of up to $\pm 280 \, \mathrm{km \, s^{-1}}$. These are seen at different locations—the redshifted plasma is seen where the hard X-ray source is later seen (energy deposition site). In addition, blueshifted plasma shows the very early onset of the fast rise of the filament.

Key words: Sun: filaments, prominences – Sun: flares

*Supporting material:* animations

1. Introduction

Understanding the early phases of eruptions and flares is key to developing prediction strategies. A range of models that aim to describe the key early stage, which include reconnection triggering the release of a twisted flux rope through tether cutting (e.g., Moore et al. 2001), reconnection occurring above a sheared arcade to allow its release known as breakout (e.g., Antiochos et al. 1999), and instabilities such as kink or torus (e.g., Török & Kliem 2005), have been developed over many years. The behavior of filaments and their surroundings has been studied for many years, and early rising motions or absorption have been observed tens of minutes before the flare begins (e.g., Tandberg-Hanssen et al. 2005). This early phase is the key to understanding the eruption trigger and processes.

The early phases of eruptions are captured easily using imagers such as AIA (Lemen et al. 2012) on *SDO*, but it is much more challenging to capture this early phase with a spectrometer due to the smaller field of view and long duration required to build up an image. The *Hinode* EUV Imaging Spectrometer (EIS) has captured the early phases of a flare and found that the enhanced line broadening is seen in the corona before the flare at the locations where the flux rope subsequently erupts (Harra et al. 2013), and dynamics in the preflare phase have also been found both in the chromosphere and corona by Woods et al. (2017), where flows of over $100 \, \mathrm{km \, s^{-1}}$ are observed. These two examples were both captured with spectral images built up through rastering, which takes many minutes in most cases.

Spectroscopic information is clearly of great relevance to constraining the physical models of flares. Combining imager

data and spectroscopic data has worked reasonably well in the past. However, an alternative approach is to use wide slots to produce "overlappograms" such as those produced by the NRL XUV spectroheliograph on board *Skylab* (Tousey et al. 1977). These data produced spectrally pure images, allowing simultaneous studies of hot and cold lines, and the ability to extract spectral information over a large field of view. Using these data, Cheng (1977) found large turbulent mass motions in Fe XXIV of the order of $100–160 \, \mathrm{km \, s^{-1}}$ during a solar flare. Using the same data set, Widing & Dere (1977) showed very small Doppler velocities of the Fe XXI line, indicating a stationary hot plasma region. These works demonstrate the potential of the "overlappogram" style data in providing spectral information over a large field of view. A different technique of using multi-slits was developed by Martin et al. (1974) for a ground-based system with the aim to obtain spectra in a rapidly changing circumstance such as a flare or filament eruption. The 30 parallel slits allow good spatial coverage of the Hα spectra, which made it easy to determine which part of the flare was most energetic, and where the filaments were activated in the early stages. Instruments for rocket flights have been developed over the years to produce high time resolution spectra, and having a co-alignment slot "dumb-bell" (e.g., Brosius et al. 2014).

In more recent times, Innes et al. (2008) have made use of the *Hinode*/EIS 40″ slot data to explore explosive events in an active region, measuring speeds of up 220 km s^{-1} in the He II slot image. These are observed as brightenings along the dispersion axes—which appear as horizontal brightenings in the image. A recent new design has been tested during two
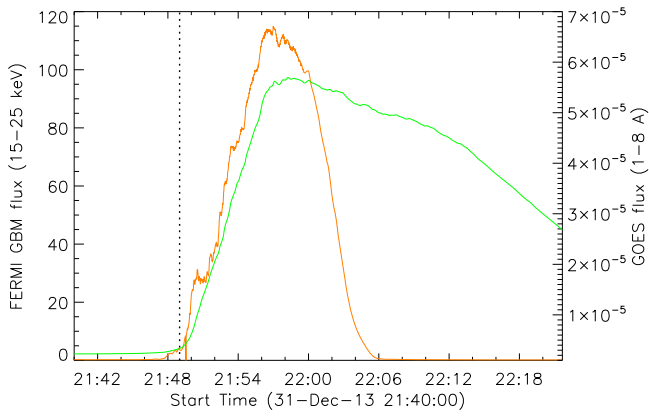
Figure 1. *GOES* light curve shown in green, and the *Fermi* light curve shown in red. The dashed vertical line shows when the EIS data mode changes from slot mode to raster mode. This happens in the very early stages of the flare rise.

rocket flights—the Multi-Order Solar EUV spectrograph. This technique allows velocity information to be extracted. During the first rocket flight, an explosive event was observed and the velocity found to be 75 km s^{-1} (Fox et al. 2010). The *Hinode*/EIS slot data have also been used by Ugarte-Urra & Warren (2011) to understand the temperature dependence of dynamics within active region upflow regions. The EIS instrument has a wider slot (266″), which acts more like a spectroheliogram and is used as the basis of the EIS flare trigger. The flare trigger mode relies on detecting a rapid increase in intensity for a single wavelength (which is efficient for telemetry use). Once a certain intensity threshold level is reached, the observing program switches to a previously selected raster mode. The slot data are ideal for this usage, as only one wavelength is needed, and it has been found that the He II emission line responds most rapidly. However, this does mean that the flare raster data misses the key early onset stage. In this paper, we make the first attempt to extract spectral information from the EIS slot data at the key early stages of the eruption.

2. Analysis

The *Hinode*/EIS (Culhane et al. 2007) is a scanning slit spectrometer that observes in two wavebands in the EUV: 170–210 Å and 250–290 Å. The spectral sampling is 0.0223 Å/pixel. There are two slits and two slots—1″, 2″ and 40″ and 266″. The 1″, 2″ slits are used for detailed spectroscopy, and images are built up through "rastering." The 40″ and 266″ apertures are slots that provide an "overlappogram" style of data where the spatial and spectral information are convolved. The 40″ slot size was chosen so that a few key emission lines would be spectrally pure. The 40″ slot includes emission over 0.9 Å. The 266″ slot covers a larger spectral range and has the advantage of covering a larger spatial area. It includes emission over 6 Å. The 266″ data have been used very effectively in the EIS flare trigger. The data covers the full field of view of the active region with fast cadence ($\approx$1 minute) for a spectrometer. The exposure time is 5 s. The data are processed and once the intensity of a region exceeds a certain level, a trigger is issued and the required new study begins. This is often a raster over the active region. The EIS study name in this example is "Flare266_Hunter01." These studies can be explored on the *Hinode* EIS Web site, http://solarb.mssl.ucl.ac.uk/SolarB/estudylist.jsp. Searching for "Flare266_Hunter01" will provide a list of when EIS has used this particular study for

flare hunting. Other flare hunting studies exist such as "Flare266_Hunter02" and "Flare266_Hunter03."

We analyze an example of the flare trigger data on 2013 December 31 (SOL2013-12-31). The *GOES* (Chamberlin et al. 2009) and *FERMI* (Atwood et al. 2009) light curves are shown in Figure 1, where the vertical dashed line highlights the time when the mode switched from flare search study (the EIS 266″ slot data) to flare study (EIS raster data). We checked all the GBO detectors for evidence of saturation, and the data plotted in Figure 1 are from a detector that did not appear to show significant evidence of saturation. Since the dotted line is early in the rise, we would not expect a large HXR flux, but there is clearly a rising signal in the 15–25 keV range at this time, although the scale perhaps makes it a little hard to see. The trigger was issued at 21:49:50 UT. We analyzed 13 minutes of slot data before the flare trigger was initiated. The slot data observed only in the He II 256 Å emission line, and the 266″ slot is equivalent to a wavelength range from 252 to 260 Å. Detailed line lists are described in Brown et al. (2008). There are significant emission lines within the slot wavelength range that we will consider and describe later.

SDO/AIA (Lemen et al. 2012) observes the Sun in seven EUV and three UV channels with a pixel size of 0.″6 and a time cadence of 12 s. AIA data were analyzed in the 304 Å channel so that they could be easily co-aligned with the EIS 256 Å data. A detailed analysis of the AIA responses in each channel is provided by O'Dwyer et al. (2010). In the 304 Å band, the He II emission line is dominant in both active regions (with some contamination from Si XI) and flares (with minor contribution from Ca XVII).

The EIS slot data and the AIA 304 Å data were co-aligned initially by feature recognition using data sets well before the flare begins at 21:39 UT. A cross-correlation was done between the images to optimize the alignment. This was more challenging than normal since the slot data has spectral "blurring" along the dispersion axis. However, we estimate that it is accurate to within 2″. Figure 8 shows the contours of the AIA convolved data overlaid on the EIS slot data to provide some visual confidence that the alignment is reasonable.

3. Results

The first stage of analysis was to demonstrate what emission lines are likely to exist in the slot wavelength range during a flare. This is potentially challenging since our data covers the preflare period (where we can assume active region behavior) but also includes the start of the flare rise phase (when EUV emission starts to change rapidly). We studied both active region and flare spectra to encompass both intensity regimes. The synthetic spectra were determined from CHIANTI (Landi et al. 2013) using the available active region differential emission measure (DEM) and a flare DEM. These spectra are shown on the left-hand side of Figure 2. It is clear that there could be significant differences in the intensity ratios of emission lines in each case, and indeed the most obvious difference is that the flare emission line, Fe XXIV, becomes dominant. The He II emission line in this band has been known for decades to be notoriously difficult to model, and so is not dominant in the synthesized data—this problem has been described by Golding et al. (2017). CHIANTI includes optically thin lines, so He II is not fully accounted for. Being aware of this problem, alongside the fact that the slot data are
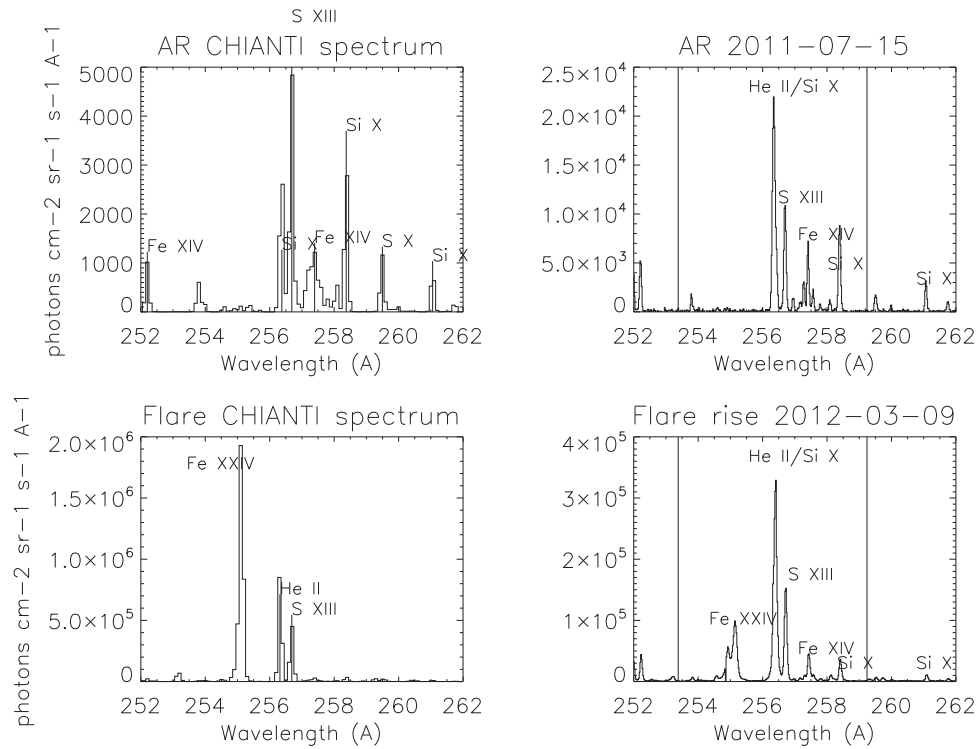
Figure 2. Examples of four spectra: the top row shows an example active region spectra with the left panel derived from CHIANTI, and the right panel from the full CCD active region data from EIS. The bottom row shows the flare spectra: the left image is from CHIANTI and the right image is a spectrum taken on 2012 March 9 03:27 UT during the impulsive phase of a flare when a full CCD scan was carried out. All spectra are plotted over the wavelength range seen by the wide slot, with the two vertical lines highlighting the range. The key emission lines during the flare are He II, S XIII, and Fe XXIV.

from very early in the flare event and so will not necessarily have reached high enough temperatures for the classic flare lines to show, we studied two full CCD data sets—one from a flare in the early stage and one from an active region. The full CCD data are not used often due to the high telemetry demands but are a great source of information, and cover the full spectral range of the slot data. The right-hand side of Figure 2 shows a subset of the full CCD spectrum showing the wavelength range that is covered by the wide slot. A standard non-flaring active region data set was studied, and in this it can be seen that the He II/Si X blend is dominant. For a flare example, we used a rare EIS observation with full spectra that was made during the M class flare on 2012 March 9 which has been analyzed by Doschek et al. (2013). The flare started at 03:24 UT (as seen in *GOES*), and we studied the slit position in the bright core at 03:27UT. This was a few minutes into the impulsive phase at this stage, when the Fe XXIV line is not dominant. It is clear from this figure that the He II 256 Å (blended with Si X) is still the strongest emission line. The Si X impact on the He II line can be estimated by understanding the intensity of the Si X 256.36 Å. The ratio of Si X 256.36/261.04 Å is constant and is approximately 1.1 as determined from CHIANTI (Landi et al. 2013). The Si X 261.04 Å emission line is weak (see Figure 2) so we assume that the impact of Si X 256.36 Å on He II is also insignificant. The Fe XXIV emission was weaker in the full CCD data than in CHIANTI—this is likely to be due to the fact that the DEM is the one covering the peak of the flare, whereas the EIS full spectral data is in the early stages. Due to the wavelength separation of Fe XXIV and He II, this should be obvious in the slot data. We will discuss this later. We use the full CCD data sets to give us a good idea of what emission lines are dominant during a flare and in an active region so that we

Table 1
Relative Intensities of the AIA Bands Chosen to Replicate the Emission Lines in the EIS Slot Band

	Ion	% Intensities Applied to AIA Images
	Ion Ratios Applied to AIA Bands	
Flare	Fe XXIV	30% (131)
	He II	100% (304)
	S XIII	46% (335)
	Fe XIV	13% (193)
	Si X	11% (193)
Active Region	He II	100% (304)
	S XIII	50% (335)
	Fe XIV	30% (193)
	Si X	36% (193)

Note. The He II emission line, as the strongest line, is chosen to be 100%. These are shown for both the flare and the active region case. The filter bands from AIA that were chosen to be the closest in temperature to each EIS emission line is shown in brackets in the right-hand column.

can then apply the intensity ratios of the emission lines in the EIS slot band to convolve synthetic EIS slot data from the AIA data. We can never be completely sure of what these intensity ratios are without simultaneous spectral data, which are not available. Hence, we make an assumption that the spectral line intensities at the early flare stage are similar to those in a different flare when a full CCD spectrum was available. As will be seen later on, we concentrate on the strongest regions in the slot data that we assume to be He II. The ratios of the other lines are not that key to the analysis of the bright regions, but it is nonetheless interesting to know what is in the band.
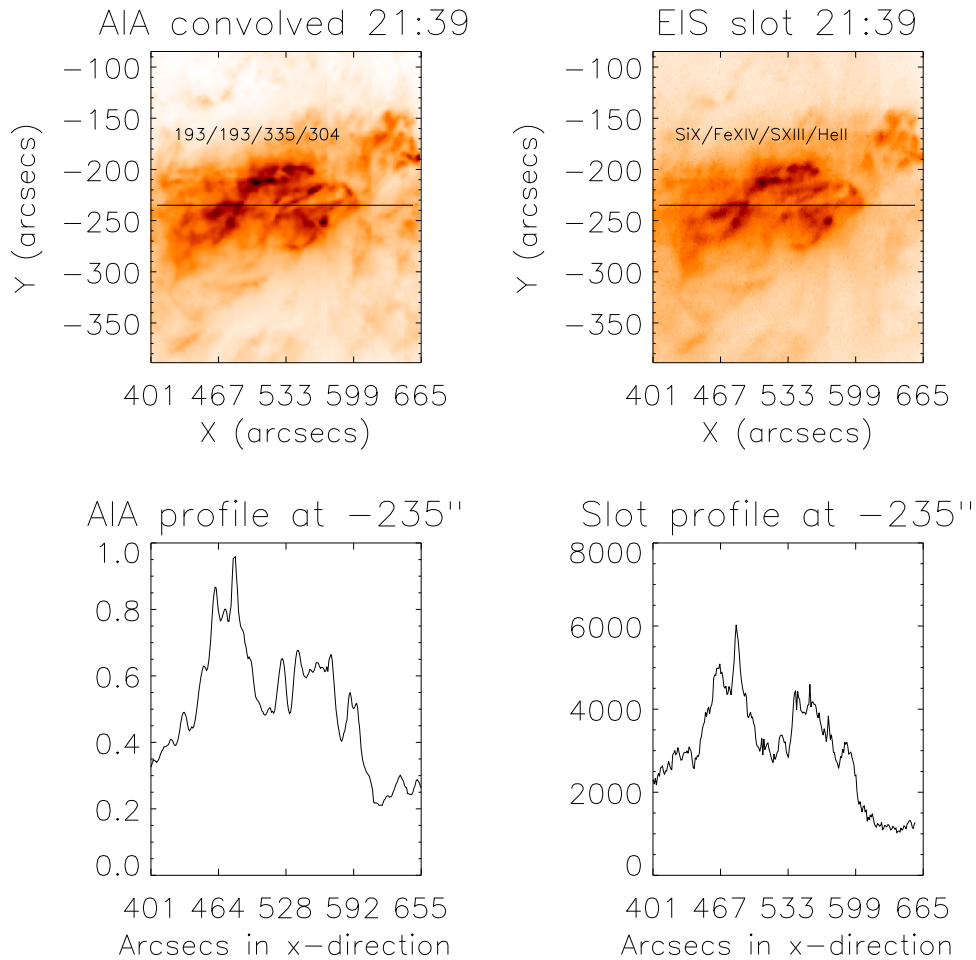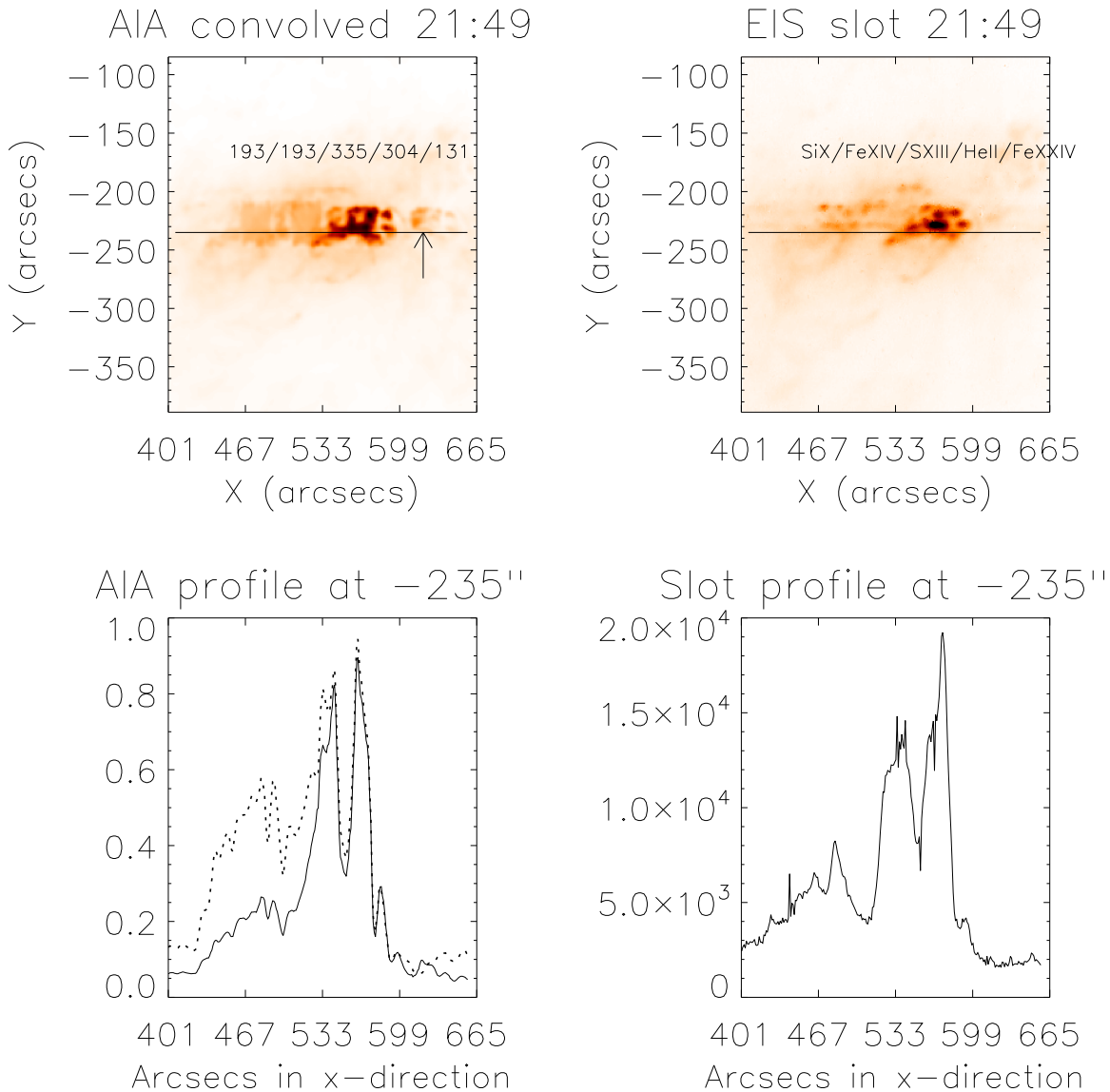
Figure 3. Active region data before the flare begins.The top row shows convolved AIA data on the left and the EIS slot data on the right. On the AIA convolved data, the labels show the filters used to emulate the emission lines seen in the EIS slot data. The labels on the EIS slot image highlight the order of the emission lines seen in the slot band. The dispersion axis of EIS is from right to left and hence the wavelength is "reversed." The bottom row shows profiles along the images at $y = -235''$. The similarity in the behavior of the profiles indicates that the approximate ratios of the emission lines selected are reasonable.

We now check whether our assumption that the emission lines in the bands are those of the full CCD active region data for all of the slot data, except for the last one, which is at 21:49 UT. This one is just as the flare starts and an intensity increase is observed. For this last slot image, we assume the intensity ratios of the flare's full CCD spectrum shown in Figure 2. In order to produce synthetic EIS slot data from the AIA images, we carry out the following steps. The AIA data were degraded using a PSF of $3''\!.5$ (Young et al. 2013) to replicate the EIS spatial resolution. The AIA data were normalized. We use proxies of each emission line in Figure 2 to create an "overlappogram" from AIA data. We use the 131 Å channel (Fe XXI + weak Fe XXIII) to replicate Fe XXIV, 304 Å (He II) to replicate He II, the 335 Å channel (Fe XVI + weak FeXIV) to replicate S XIII, the 193 Å channel (Fe XII) to replicate Fe XIV, and the 193 Å channel to replicate Si X. We have chosen the AIA bands that are closest in temperature to the emission line using the work of O'Dwyer et al. (2010). We use the intensity ratios of the emission lines in Figure 2 on the right-hand side. The relative intensities of these lines are illustrated in Table 1. We convolve each AIA image by shifting it by the appropriate amount along the EIS dispersion axis relative to the He II emission line. This creates a pseudo "overlappogram." An active region example is shown in Figure 3. The top row shows the convolved AIA image beside the EIS slot image. A visual

inspection shows that the images are very similar. The labels on the plot highlight the order of the emission line images, with the appropriate "overlapped" images for each spectral line. These are shifted along the dispersion axis, which is from right to left in the x-axis (hence the location of the emission is opposite to that seen in the spectra). The AIA image has each "overlapped" image labelled in order of what filter band was used to replicate each EIS emission line. Below the images are intensity profiles along $y = -235''$. Both AIA and the slot data show similar behavior, with the same number of peaks. So, we can be confident that the convolution is working well.

We carried out the same process for the flare slot data, and the results are shown in Figure 4. The convolved AIA and the EIS slot images look reasonably similar—the biggest difference is the feature on the right-hand side of the convolved AIA data that is the image of 131 Å shifted to the wavelength of Fe XXIV. This is highlighted with an arrow. This is not seen as strongly in the EIS slot data, so we can assume that Fe XXIV is weaker than we deduced from the data in Figure 2. We highlight here that the assumption made can never be perfect without simultaneous spectra, which are currently unavailable. It is known that flares will be different from each other, and in the early stages the EUV spectra will change rapidly, so it is not surprising that we see this difference. The profiles along $y = -235''$ are also shown. As with the active region example,

Figure 4. Flare data in the rise phase. The top row shows convolved AIA data on the left and the EIS slot data on the right. On the AIA convolved data, the labels show the filters used to emulate the emission lines seen in the EIS slot data. An arrow highlights where the Fe XXIV data is, and it is more enhanced from our assumptions than compared to the EIS slot data. The labels on the EIS slot image highlight the location of the emission lines seen in the slot band. The flare data has an additional Fe XXIV emission line that becomes strong. The dispersion axis of EIS is from right to left and hence the wavelength is "reversed." The bottom row shows profiles along the images at $y = -235''$. The AIA profile also shows what the profile would look like by assuming the active region ratios in Figure 3 (shown as a dotted line). Our assumptions for the flare are a much better fit to the slot data. The similarity in the behavior of the profiles indicates that the approximate ratios of the emission lines selected is reasonable. It is noted that the largest peaks in the EIS slot data are showing a broader FWHM than the equivalent of those seen in AIA. This is indicating broadening in the dispersion direction in EIS related to dynamics.

the same number of peaks is seen in the AIA and EIS slot, with similar relative intensities. The AIA profile is also shown using the active region ratio assumptions that were used in Figure 3. The assumptions used for the flare are close to the slot data. A key point is that the strongest peaks do not change significantly, irrespective of our assumptions, since He II is dominating in both cases. By using the convolved AIA data, we aim to account for the spatial changes occurring in the early flare stages.

A distinctive difference can be seen between the AIA convolved data and the slot data, in that the EIS slot data are showing wider FWHM than the convolved AIA. This indicates that the emission lines are broadened and/or shifted in this passband. This would be expected at this stage of the flare. We will explore this further.

The AIA and EIS data are shown in Figures 5 and 6. The EIS slot data analyzed starts at 21:37:09 UT and the new study initiated by the flare trigger starts at 21:49:33 UT. The flare starts at 21:47 UT as seen in *GOES*, so the slot data exist during the very early stages of the flare, in the first two minutes. Figures 5 and 6 show the EIS slot data and the AIA data over a period of 20 minutes in order to show the preflare and eruption phases. Animated versions are available, with the AIA animation showing the filament eruption occurring. A height–time analysis of the filament eruption was carried out by measuring the brightest front in the AIA data (see Figure 7). It was found to erupt with a plane-of-sky speed of $148 \, \mathrm{km \, s^{-1}}$. The times for each of the EIS slot images are highlighted on the plot, emphasizing the good time cadence for this spectral data compared with rastering spectral data.
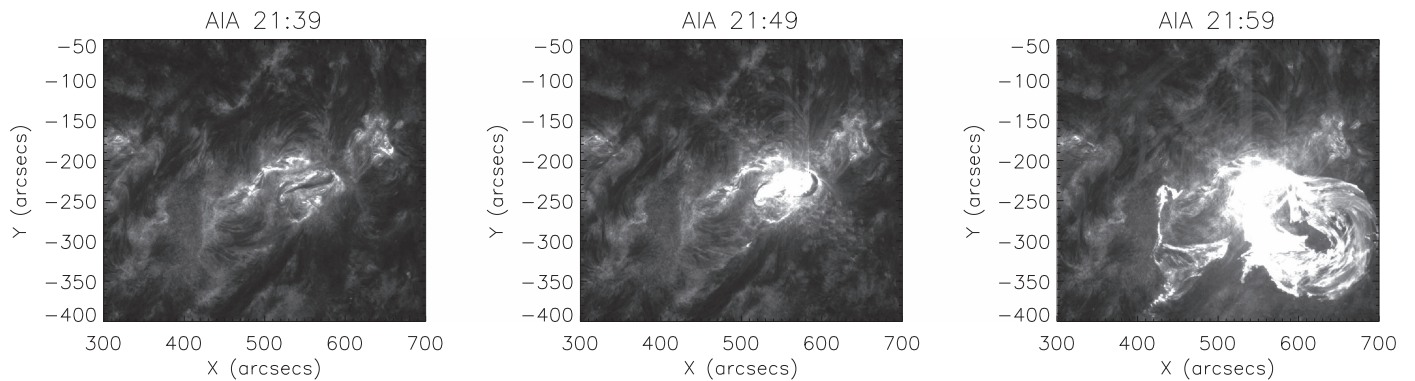
Figure 5. He II 304 Å image at three times. At 21:39 UT, a dark filament can be seen in the center of the bright active region. By 21:59 UT, the eruption is well under way. The animated version of this figure runs from 21:15 to 21:59 UT.

(An animation of this figure is available.)
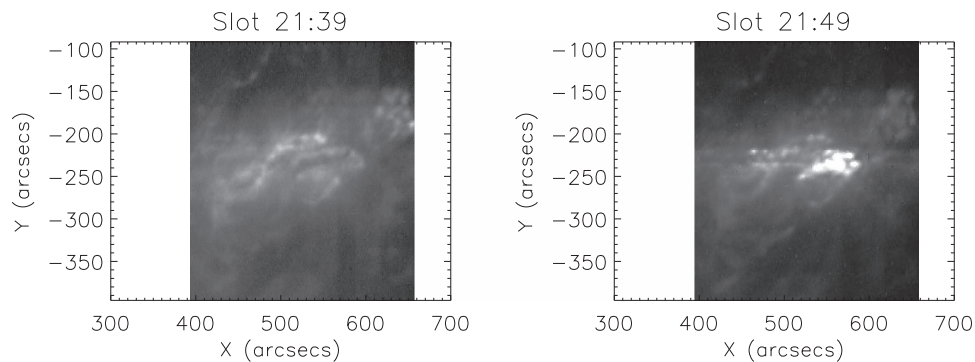
Figure 6. EIS He II 256 Å data for 21:39 UT and 21:49 UT. The latter image is the last slot image before EIS switched to raster mode. The full sequence from 21:39 to 21:49 UT is shown in the animated version of this figure.

(An animation of this figure is available.)
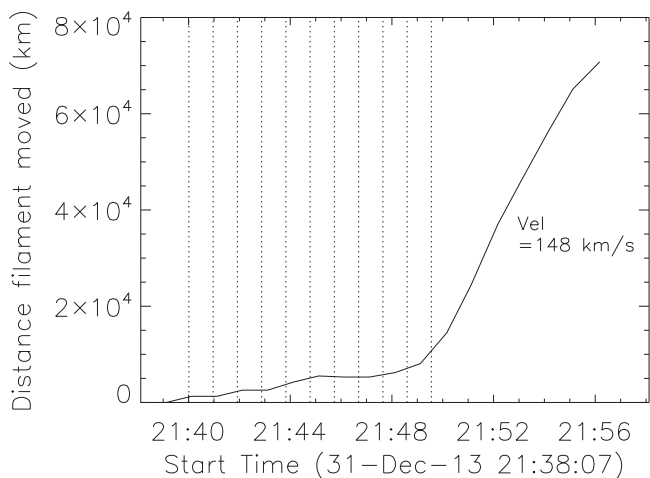
Figure 7. Height–time plot for the AIA filament eruption, tracking the brightest edge of the feature as seen in the 304 Å filter band. The vertical dashed lines highlight when each slot image was taken. The profile shows a slow rise, followed by a fast rise, as has been typically seen. The fast rise phase reaches a speed of 148 km s^{-1}.

We looked at the time series of the EIS slot data. Examples of this are shown in Figure 8. We study the profiles at the brightest region in the preflare data that is toward the center of the slot image. We assume that this bright feature is dominantly from He II. The first three times shown have similar behavior for the profiles of AIA and the EIS slot data. A difference that is seen is that the peak of the EIS slot data starts to show a shift,

which equates to a redshift. This increases significantly in the slot data at 21:49 UT.

In order to explore this further, we studied the last slot image at 21:49 UT in different regions. This is shown in Figure 9, where the profiles at a y location of $-218''$, $-230''$, $-235''$, $-241''$ are displayed. We choose these regions as they are over the brightest spots seen in AIA 304 Å. It is also clearly seen that the profiles are broader in the EIS slot data than in the convolved AIA data, which is to be expected since the slot data have both spectral and spatial information combined. If a feature is observed to be extended in the x-direction, then this is likely to be a broadening or shifting of the spectral emission line. The convolved AIA and slot profiles show similar features, and so the assumptions from the convolution (the spatial resolution and the emission line intensities used) appear to work well. This indicates that the assumptions used are reasonable. The most intense peaks are due predominantly to the strong He II emission line, and we concentrate on these regions next. We keep in mind that the S XIII emission line is weaker than the He II line and lies to the long wavelength side. Although it is weaker, it is still significant. However, the wavelength difference would lead to a shift of the order of 420 km s^{-1}, which is very large and should be clearly seen in the data. The short wavelength side of the He II line has no significant contribution from any emission lines close to it that would affect the measurement of velocity. The Fe XXIV line is too far away and should be easily identifiable in the slot data and the convolved AIA data.

6
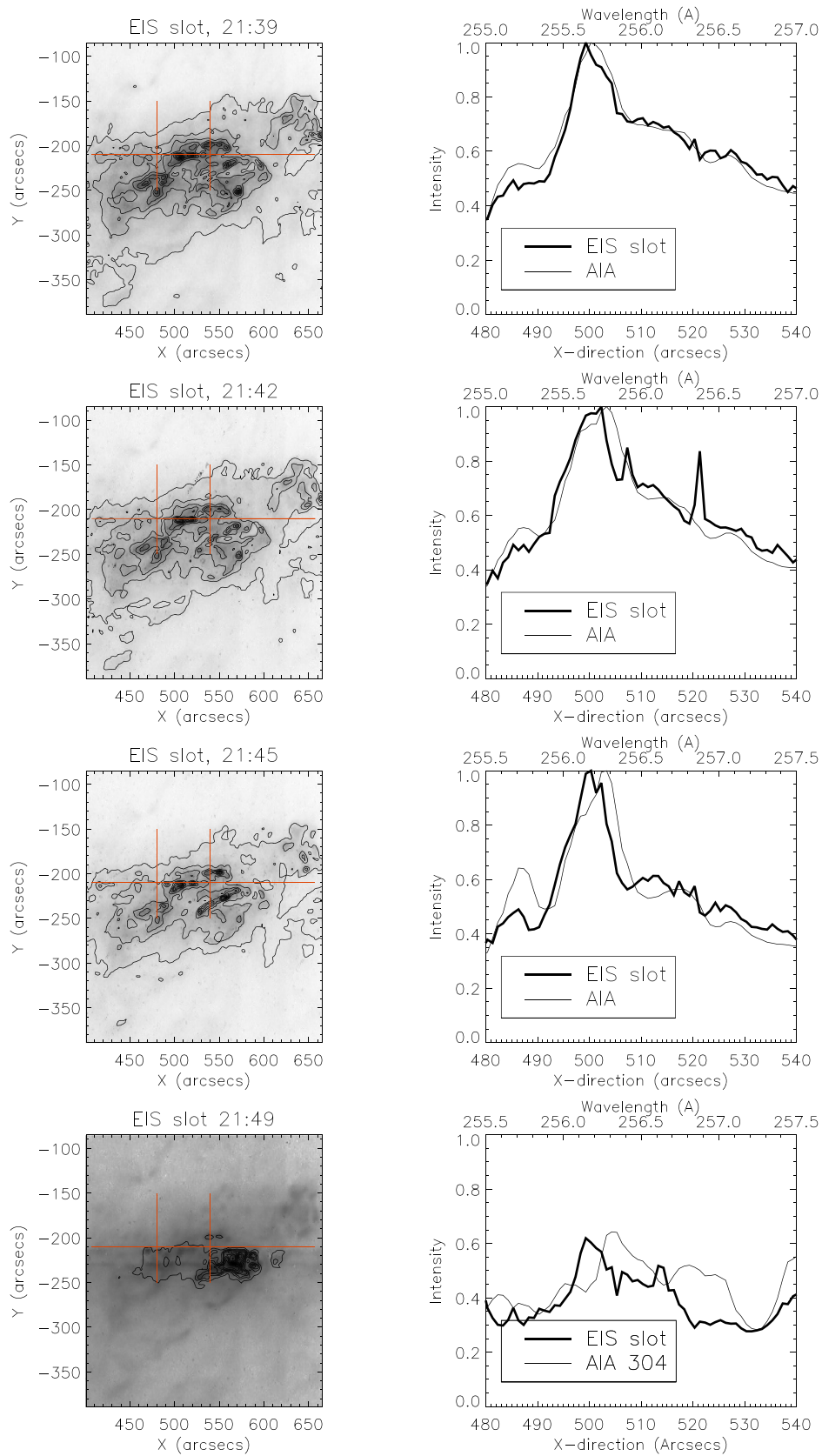
Figure 8. Series of EIS slot images and profiles along $y = -210''$. On the left-hand column, the EIS slot images are shown with the AIA convolved images as overlaid contours. This illustrates that the alignment is good. The last image at 21:29 is shown in logarithmic scale. On each of these images, a red horizontal line highlights the y-direction that the profile is determined from and the two short vertical lines illustrate the range in the x-direction. We concentrate on the brightest region from the early phases. On the right-hand side, we plot the normalized intensity profile of the slot data as a thick line. The AIA convolved intensity profile is shown as a thin black line.
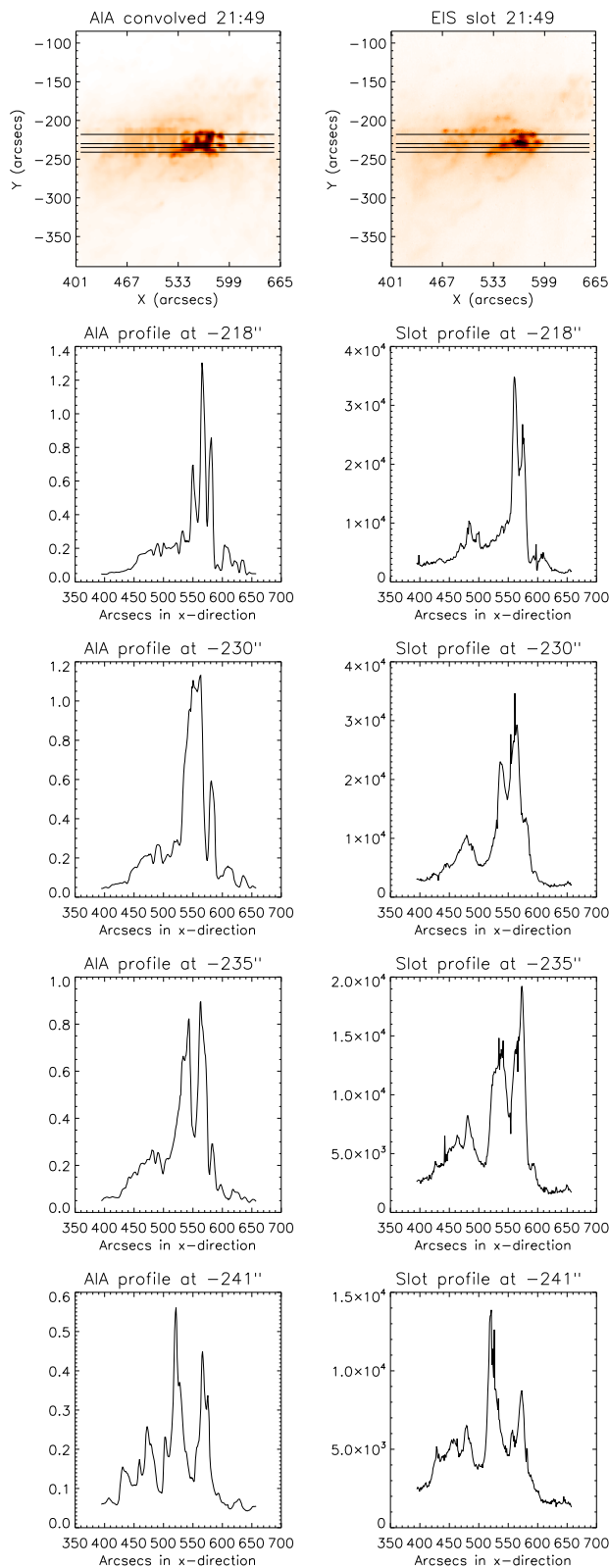
Figure 9. Top-left figure shows AIA convolved data (at the EIS spatial resolution and convolved to replicate the emission lines in the EIS slot band), the top-right figure shows the EIS slot data at 21:49 UT, which was the last image before the mode switched to raster mode. The four solid horizontal black lines show the locations of interest. The following four rows show the intensity profile of the AIA 304 Å data along the black line on the left and the equivalent profile from the slot data on the right.
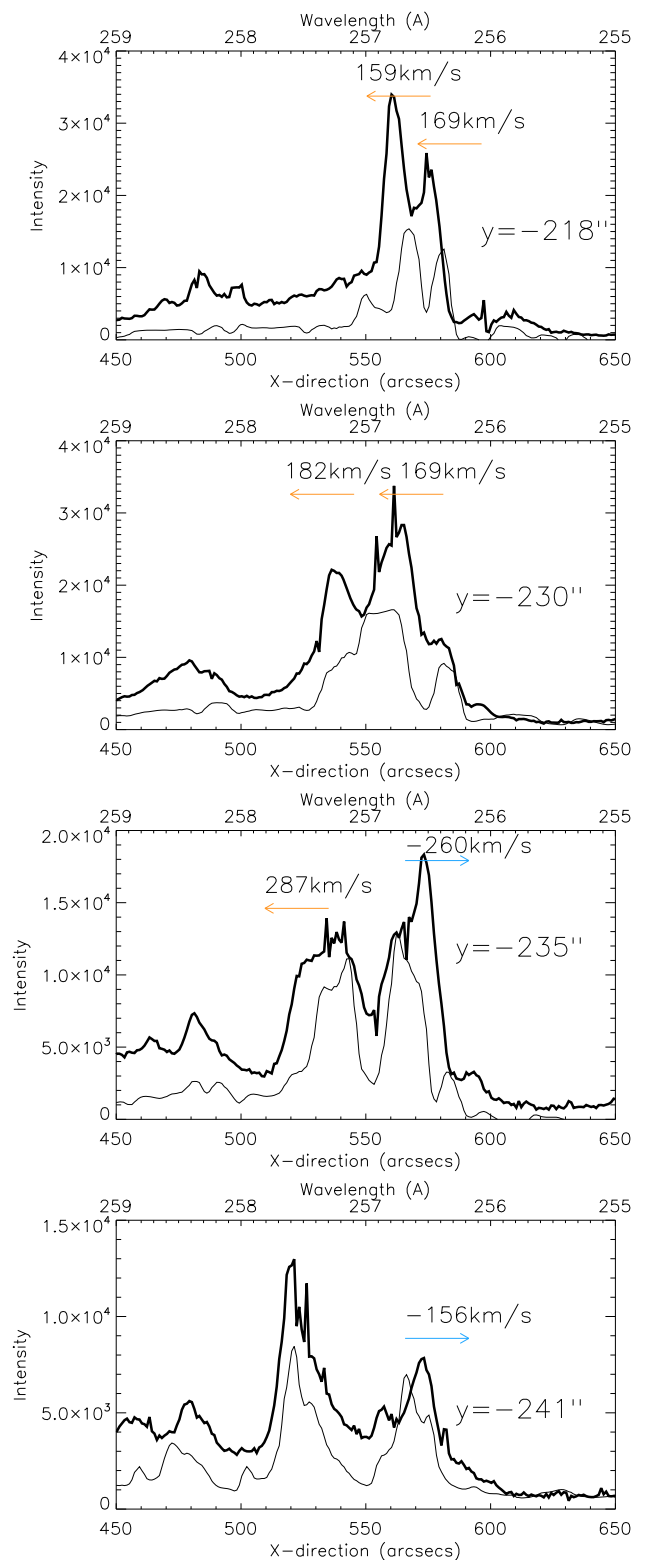
Figure 10. Each image shows a zoom-in of the slot and AIA profiles shown in Figure 9 at 21:49 UT. The EIS slot data are shown as the thicker line. The wavelength scale is shown for reference (the dispersion direction is to the left), defined for the central pixel. The wavelength range will change depending on which spectral feature is being analyzed—we plot it to illustrate the dispersion direction. Making comparisons of the peaks of each feature, we can determine if there is a red- or a blueshift flow. Arrows are shown above each strong peak and are color-coded as to whether they show a blue- or a redshift. The values of the velocities are shown beside the features.
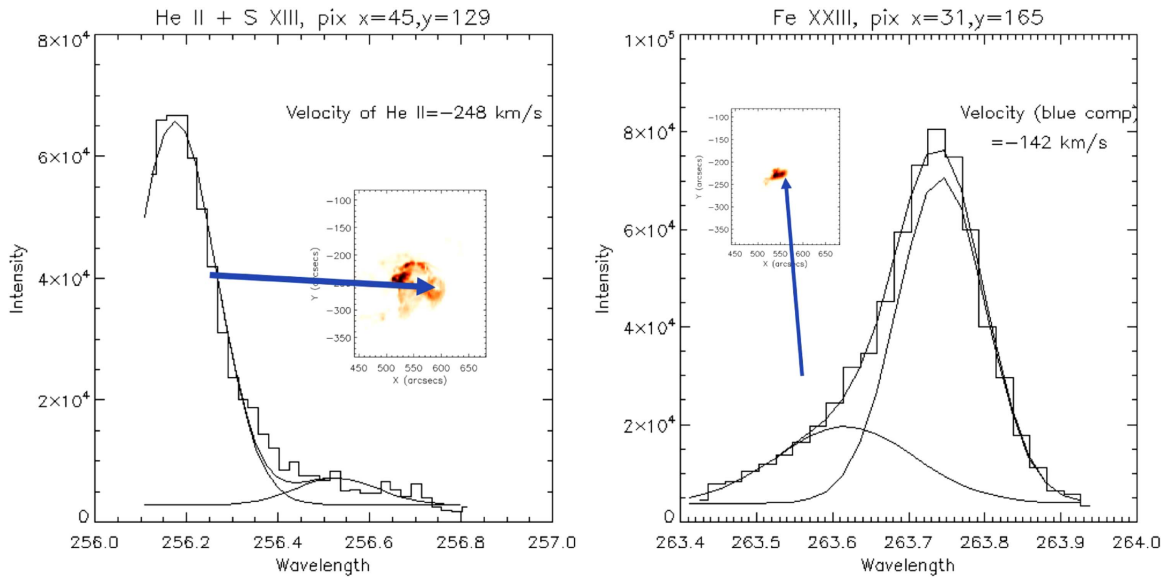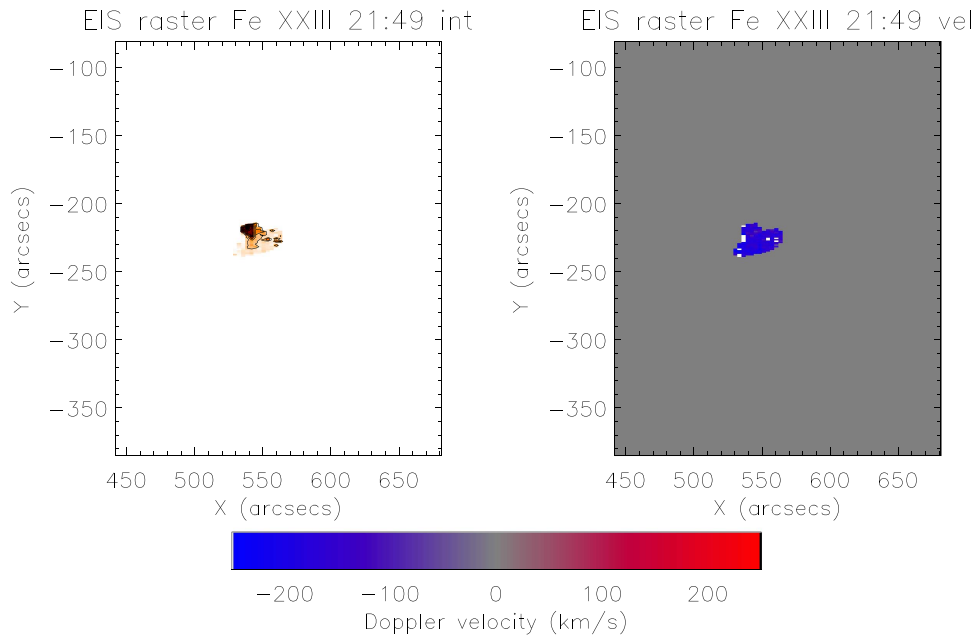
Figure 11. Left figure shows an example of the He II and S XII line profiles, with the inset image showing the location of the spectrum. In this case it was in the filament eruption itself. The right-hand profile shows the Fe XXIII emission line, which has a two-component fit. The speed of the blueshifted component is 142 km s^{-1}, and it is located at the end of the post-flare loops.
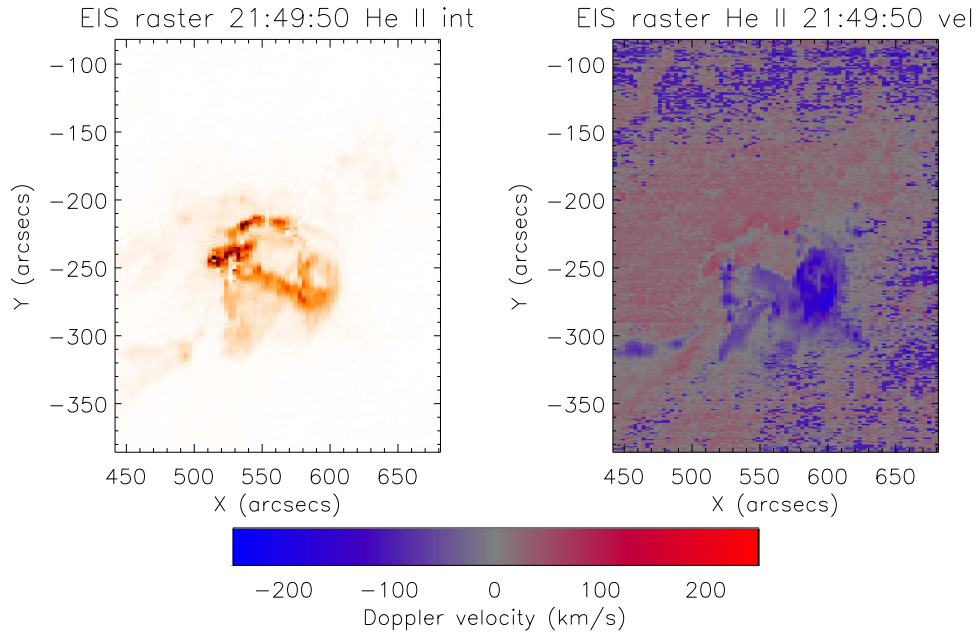
Figure 12. Left figure shows an example of the He II line intensity image. The right-hand image shows the Doppler velocity measurements of the He II emission line. The color bar shows the range of the Doppler velocity with the strongest blueshifted velocities occurring at the filament eruption.

Figure 10 shows a plot focused only on the brightest and broadest features at each of the horizontal lines shown in Figure 9. We assume that the brightest features are dominated by He II. It is seen that the EIS slot data are broader in most cases than the AIA data, although the AIA data were degraded in resolution to match that of EIS. The slot and AIA data were aligned before the flare began, and we assume that this alignment provides the rest wavelength. A feature that deviates from this must be showing a flow. To determine the velocity, we measure the number of pixels that the peaks of the convolved AIA profiles and the EIS slot data differ by. The results of this (shown in Figure 10) are that both red- and blueshifts are seen in different regions. The most interesting

feature is at $y = -235''$, where the two peaks are seen, illustrating opposite directions of flowing plasma. This is a region along the filament eruption and could indicate untwisting. Farther south at $y = -241''$ shows a strong blueshift of -156 km s^{-1} located in the direction where the filament is erupting. We can visually observe the filament erupting in AIA and can measure the speed in the plane of the sky. There was evidence of a slow rise at 21:46 UT, and then a fast rise started at 21:49 UT (see the animated versions of Figures 5 and 6). This is similar to observations by Sterling & Moore (2005) who found a slow rise phase that lasted about ten minutes with a speed of ≈ 15 km s^{-1}, followed by a fast rise phase with a speed of 200 km s^{-1}. The EIS slot data show speeds of ≈ 156 km s^{-1}

Figure 13. Left figure shows an example of the Fe XXIII line intensity image, with the blueshifted component intensity shown as the image, and the main emission line shown as contours. The right-hand image shows the Doppler velocity measurements of the Fe XXIII blueshifted component only.

in the first minute of the fast rise phase. It is clear that this plasma is moving, and we can observe that movement along the dispersion axis in the EIS data. This is consistent with the measurement of the speed of the fast rise phase from AIA, except the spectral data allow a measurement in the very early stages. The redshifted features farther north at $y = -218''$ and $y = -230''$ is close to where the post-flare loops form (see the animated versions of Figures 5 and 6). It is possible that this may be downflow associated with energy deposition. *RHESSI* data were unavailable during the rise and peak of the impulsive phase, but show a single 12–25 keV source at 22:11:40 UT located at $(552'', -233'')$, in the southern flare ribbon, and so is consistent with the location of downflows. It is also interesting that the redshifts begin to show in this region before the flare rise begins.

In order to check the location of chromospheric evaporation and the erupting filament, we made use of the raster data that followed the slot data. We then analyzed the raster data that followed the slot data. The raster started at 21:49:50 UT and finished at 21:58:42 UT (just after the peak of the flare), and hence covers most of the impulsive phase. We analyzed the profiles of He II (and its neighbor S XIII) and Fe XXIII. The profile of the He II data as the filament was already clearly erupting is shown in Figure 11. The extended feature marked by an arrow is the filament erupting as seen through raster imaging. The image is built up by rastering from right to left. We choose one of the most blueshifted profiles, which equated to a speed of 248 km s^{-1}. This is similar in speed to the feature seen at $y = -235''$ in the slot data. As can be seen from Figure 11, the spectral line is partly shifted out of the spectral window. The Fe XXIII line was fitted with a two-component fit, and in Figure 11 we show one of the fastest speeds measured. The Fe XXIII line showed a strong blue asymmetry and was located in the region where the post-flare loops formed toward the footpoints of the flare loops. A blueshifted velocity of 142 km s^{-1} was measured, which is consistent with that measured in Doschek et al. (2013). The location of the strong

blueshifted feature showing chromospheric evaporation is spatially close to where we see the bright features we analyze in the slot data. This indicates that the redshifted emission that we estimate in the slot data could be related to early chromospheric evaporation, with downflows being seen at the footpoints in the chromosphere He II emission line. The intensity and Doppler velocity maps for He II are shown in Figure 12. This highlights the strong flows seen as the filament erupts and moves away from the disk. This is exactly what we measure in the very early stages with the slot data, but without the need to raster. The flare footpoints that are highlighted in Figure 13 show the intensity and Doppler velocity of the blue component of the spectral line only. We assume that this blueshift is caused by evaporating plasma, as has been seen in previous works. The earlier He II slot data show clear downflows in this region, as would be expected in the chromosphere related to energy deposition, as would be expected in the chromosphere.

4. Conclusion

We perform the first analysis of the 266$''$ slot data from *Hinode* EIS, along with imaging data from AIA, to determine whether velocities can be extracted at the early stages of a filament eruption. We demonstrate that this can be done and find a speed consistent with that found through subsequent imaging data. The accuracy of the velocity is not high, but the locations of the high speeds can be measured over a large field of view. We found the blueshift velocity during the very early part of the filament eruption to be between 156 and 260 km s^{-1}. Interestingly, new Hα observations of a flare have been made by Cho et al. (2016), and they also found a speed range between -130 and 38 km s^{-1}, which lasts around six minutes and is consistent with the start of the rise of the filament. We also found downflows to occur in the locations where the subsequent raster data showed strong chromospheric evaporation. Our slot data provide a new way of analyzing chromospheric/transition region flows during a

filament eruption and flare. We can also see evidence of early phase activation at regions that will later become flare footpoints.

These new measurements have the potential of opening up a new way of understanding eruptions or any other high velocity events. There is a wealth of data in the archive of the 266″ slot data that we encourage users to explore.

Hinode is a Japanese mission developed and launched by ISAS/JAXA, collaborating with NAOJ as a domestic partner, and NASA and STFC(UK) as international partners. Scientific operation of the *Hinode* mission is conducted by the *Hinode* science team organized at ISAS/JAXA.

References

Antiochos, S. K., DeVore, C. R., & Klimchuk, J. A. 1999, ApJ, 510, 485
Atwood, W. B., Abdo, A. A., Ackermann, M., et al. 2009, ApJ, 697, 1071
Brosius, J. W., Daw, A. N., & Rabin, D. M. 2014, ApJ, 790, 112
Brown, C. M., Feldman, U., Seely, J. F., Korendyke, C. M., & Hara, H. 2008, ApJS, 176, 511
Chamberlin, P. C., Woods, T. N., Eparvier, F. G., & Jones, A. R. 2009, Proc. SPIE, 7483, 743802
Cheng, C. C. 1977, SoPh, 55, 413
Cho, K., Lee, J., Chae, J., et al. 2016, SoPh, 291, 2391
Culhane, J. L., Harra, L. K., James, A. M., et al. 2007, PASJ, 243, 19
Doschek, G. J., Warren, H. P., Young, P. R., et al. 2013, ApJ, 767, 55
Fox, J., Kankelborg, C, & Thomas, R. J. 2010, ApJ, 719, 1132
Golding, T. P., Leenaarts, J., & Carlsson, M. 2017, A&A, 597, A102
Harra, L. K., Matthews, S. A., Culhane, J. L., et al. 2013, ApJ, 774, 122
Innes, D. E., Attie, R., Hara, H., & Madjarska, M. S. 2008, SoPh, 252, 283
Landi, E., Miralles, M. P., Raymond, J. C., & Hara, H. 2013, ApJS, 763, 86
Lemen, J. R., Title, A. M., Akin, D. J., et al. 2012, SoPh, 275, 17
Martin, S. F., Ramsey, H. E., Carroll, G. A., & Martin, D. C. 1974, SoPh, 37, 343
Moore, R. L., Sterling, A. C., Hudson, H. S., & Lemen, J. R. 2001, ApJ, 552, 883
O'Dwyer, B., Del Zanna., G., Mason, H. E., Weber, M. A., & Tripathi, D. 2010, A&A, 521, A21
Sterling, A. C., & Moore, R. L. 2005, ApJ, 630, 1148
Tandberg-Hanssen, E., Martin, S. F., & Hansen, R. T. 2005, SoPh, 65, 357
Tórök, T., & Kliem, B. 2005, ApJL, 630, L97
Tousey, R., Bartoe, J. D. F., Brueckner, G. E., & Purcell, J. D. 1977, ApOpt, 16, 870
Ugarte-Urra, I., & Warren, H. P. 2011, ApJ, 730, 37
Widing, K. G., & Dere, K. P. 1977, SoPh, 55, 431
Woods, M. M., Harra, L. K., Matthews, S. a., et al. 2017, SoPh, 292, 38
Young, P. R., Doschek, G. A., Warren, H. P., & Hara, H. 2013, ApJ, 766, 127